Self-organized Patterns in Predator-Prey Droplet Systems

Yutong Liu[+], R. Kailasham[+], Pepijn G. Moerman, Aditya S. Khair*, Lauren D. Zarzar*

Y. Liu, Dr. L. D. Zarzar
Department of Chemistry
The Pennsylvania State University
University Park, PA 16802, USA
E-mail: ldz4@psu.edu

Dr. R. Kailasham, Dr. A. S. Khair
Department of Chemical Engineering
Carnegie Mellon University
Pittsburgh, PA 15213, USA
E-mail: akhair@andrew.cmu.edu

Dr. P. G. Moerman
Department of Chemical Engineering and Chemistry
Eindhoven University of Technology
Eindhoven 5612, AP, Netherlands

Dr. L. D. Zarzar
Department of Materials Science and Engineering
The Pennsylvania State University
University Park, PA 16802, USA

[+] These authors contributed equally.
[*] Corresponding authors

Supporting information for this article is given via a link at the end of the document.

Abstract: Non-equilibrium patterns are widespread in nature and often arise from the self-organization of constituents through nonreciprocal chemotactic interactions. In this study, we demonstrate how active oil-in-water droplet mixtures with predator-prey interactions can result in a variety of self-organized patterns. By manipulating physical parameters, the droplet diameter ratio and number ratio, we identify distinct classes of patterns within a binary droplet system, rationalize the pattern formation, and quantify motilities. Experimental results are recapitulated in numerical simulations using a minimal computational model that solely incorporates chemotactic interactions and steric repulsion among the constituents. The time evolution of the patterns is investigated and chemically explained. We also investigate how patterns vary with differing interaction strength by altering surfactant composition. Leveraging insights from the binary droplet system, the framework is extended to a ternary droplet mixture composed of multiple chasing droplet pairs to create chemically directed hierarchical organization. Our findings demonstrate how rationalizable, self-organized patterns can be programmed in a chemically minimal system and provide the basis for exploration of emergent organization and higher order complexity in active colloids.

Introduction

The emergence of non-equilibrium patterns is common within living systems and often critical to organizational function [1–9]. On the macroscale, organisms self-organize with purpose; for example, emperor penguins huddle to conserve energy and maintain body temperature [1], while ants form bridges or ladders to facilitate cargo delivery and migration efficiency [2]. On the microscale, bacterial colonies evolve complex spatial organizations that enable them to collectively respond to external cues such as changes in light intensity, temperature, and oxygen concentration [3–5]. These organizations are maintained out-of-equilibrium by continuous energy expenditure, and the patterns often rely on complex interactions between group constituents [10–12]. Inspired by natural systems, non-equilibrium patterns may be designed within inanimate soft matter, such as colloidal building blocks. Such colloidal organizational patterns are similarly facilitated by the combination of attractive, repulsive and, importantly, non-reciprocal interactions between the system constituents [13–15]. Non-reciprocity is only possible when out-of-equilibrium and refers to an interaction between two entities that is an apparent violation of Newton's third law: every action elicits an equal and opposite reaction. The ability to responsively modify the configurations of non-equilibrium patterns by tuning colloidal non-equilibrium interactions could be valuable as a means to induce organization and influence bulk properties of materials [16–18], leading to potential applications including

pollutant removal [19,20], medical treatment [21], cargo delivery [22–24] and responsive optics [25,26]. Most current strategies for inducing dynamic organization in non-living synthetic soft materials rely on the use of external forces like magnetic or electrical fields [27–32], rather than internal and self-adaptive forces like in-situ generated chemical gradients. Understanding how chemically fueled colloids communicate and self-organize into predictable patterns is a challenge, but progress in this space can provide fundamental insights into principles of pattern emergence and new tools for designing adaptive life-like matter.

Active droplets, which have gained notable interest recently [33–37], are a class of colloidal materials that exist far from equilibrium and are chemotactically motile in the absence of an external field. Active droplets are characterized by their propensity to move along chemical gradients that, through affecting the interfacial tensions of the droplets, induce Marangoni flows. Most research in this realm focuses on the self-propulsion properties of single droplets fueled by micelle-mediated solubilization, wherein solubilizate-filled micelles are associated with higher interfacial tensions [35]. There are a few examples of collective effects due to many-body interactions among active droplets. One such example by Maass et al. describes how hexagonal clusters of self-propelled oil droplets are formed due to hydrodynamic effects [38,39]. The size and spacing of the clusters vary with physical parameters including buoyancy of the droplets and confinement dimensions [38]. Another example by Meredith et al. is a mixture of two types of oil-in-water droplets which display predator-prey non-reciprocal interactions and self-organize into clusters that have symmetry-dependent dynamics [40]. The chemotactic non-reciprocity between the droplets arises because the surfactant preferentially solubilizes one oil (i.e. the “source”), and some source oil is transferred into the other drop species (i.e. the “sink”). Compositional ripening driven by the free energy of mixing sustains this directional oil transfer. This net directional chemical transfer thus precipitates a non-reciprocal chemotactic interaction between the two droplets, in which the source droplet usually acts as a “predator” and chases after the sink droplet “prey”. A natural question, then, is to wonder how a collection of many such predator-prey droplets would move, self-organize, and what emergent dynamic behaviors would evolve. There is a paucity of experiments on pattern-formation in such source-sink systems, although several recent computational and theoretical studies on this topic exist [14,41–45]. Here, we experimentally explore the spatial organization and dynamics of source-sink droplets, present a minimal computational model that qualitatively captures the observed trends, and yield insight into harnessing active colloids for non-equilibrium organization.

In this report, we explore how non-reciprocal chemotaxis in a binary mixture of oil droplets leads to self-organization behaviors and tunable pattern formation. We investigate systems of bromooctane (BrOct) and ethoxynonafluorobutane (EFB) droplets in aqueous nonionic surfactants, Triton X-100 and Capstone FS-30. In Triton X-100 surfactant solution, BrOct droplets are predators and EFB droplets are prey. By varying the physical inputs (droplet diameter ratios and number ratios) under conditions of consistent droplet chemistry, distinct self-organized patterns emerge. We qualitatively discuss the chemical rationale behind the pattern formation and quantitatively distinguish the patterns by counting droplet neighbors and analyzing the droplet motility. Apart from physical parameters, surfactant composition is also found to affect the pattern formation. Adding Capstone FS-30 fluorosurfactant enables the EFB to become a predator and BrOct the prey. Mixing Triton X-100 and Capstone FS-30 can tune the chemotactic interaction strength and the organization between BrOct and EFB [40]. An interesting phenomenon featuring a time-dependent disintegration of patterns is also observed and discussed, which relates pattern lifetime with limited capacity of the sink (prey). To rationalize and predict the structures and dynamics of the patterns, we model the collection of predator-prey droplets using a minimal computational framework [42,44,46], in which droplets either absorb or emit chemical species (solubilizate) and respond chemotactically to gradients in the solubilizate concentration. Associated with each droplet is an activity coefficient (A) that determines the net inward/outward flux of solubilizate and a mobility coefficient (M) that determines the strength of the interaction between the solubilizate and the droplet surface. The model successfully recapitulates experimentally observed patterns and collective motility under different physical parameters, indicating the robust ability of this minimal framework to capture the observed experimental trends. In testament to the generality of the predictive chemical framework elucidated in the binary oil system, we extend the framework to a ternary oil system and achieve more hierarchical patterns by choosing the appropriate chemical compositions and physical parameters. The present work provides applicable strategies for controllable nonequilibrium pattern formation and expands the design space for inducing self-organization in artificial systems independent of any external field.

Results and Discussion

Qualitative description of pattern emergence in a predator-prey droplet system

We began exploring how non-reciprocal chemotaxis in a binary mixture of droplets leads to pattern formation with an experimental system in which the two-body interactions are already well characterized [40]: bromooctane (BrOct) and ethoxynonafluorobutane (EFB) oil droplets in 0.5 wt% aqueous Triton X-100 surfactant (TX-100, critical micelle concentration CMC = 0.01 wt%) (**Figure 1a**). In this scenario, BrOct is the predator and EFB is the prey. Conveniently, these two oils have very different refractive indices (1.45 and 1.28, respectively) and thus are readily distinguishable with optical microscopy. Both oils are also denser than the continuous aqueous phase and sink to the bottom of the imaging chamber, lending to experimental ease. The motion of these droplets, therefore, is two-dimensional, confined to the plane of the bottom of the chamber. In 0.5 wt% TX-100 surfactant solution, BrOct droplets solubilize at 0.68 ± 0.05 μm/min (defined as change in diameter over time), and although they are not significantly self-propelled in isolation (drift velocity ≈ 2 μm/s), they do exhibit mutual repulsion when within approximately a couple hundred microns of each other (**Figure**

1b). EFB does not solubilize to a measurable extent in 0.5 wt% TX-100 so EFB is not self-propelled, and there are no long-ranged pairwise chemotactic interactions between EFB droplets (**Figure 1b**). The complete miscibility of the oils prompts the micelle-mediated transfer of BrOct oil into EFB, inducing a directional motion where BrOct droplets actively chase EFB [40].

To preliminarily explore what variables might influence the collective pattern formation of the droplets, we first examined the impact of droplet diameter ratio (defined as the initial diameter ratio of the two populations, d_{BrOct}/d_{EFB}) and number ratio (defined as the ratio of the initial number of drops in each population, N_{BrOct}/N_{EFB}). Using microfluidics, we generated different populations of monodisperse BrOct and EFB droplets in 0.5 wt% TX-100 with diameters in the range of 25 to 110 μm. To visualize the interactions between droplets, we pipetted a specific volume of each type of droplet (typically 0.1 to 4.0 μL) into a glass-bottom dish containing 0.5 wt% TX-100. The solution was gently swirled to randomly disperse the droplets without modifying the droplet diameter distribution. Within about 20 seconds of adding droplets to the dish, we started to acquire time-sequence optical micrographs using a transmission optical microscope at a rate of 0.5 frames per second. The camera field of view (6.7 mm × 6.7 mm) was centered on, but smaller than, the sample dish (1.9 cm diameter), so not every droplet remained in the field of view for the entirety of each experiment. Control experiments with a smaller dish and complete field of view were conducted to confirm consistency of the results presented herein, but faster convection of droplets to the edges presented challenges to longer term observation. (A detailed discussion about experimental design is in the Supporting Information).

Upon mixing BrOct and EFB droplets with similar diameters (d_{BrOct}/d_{EFB} = 1) in equal numbers (N_{BrOct}/N_{EFB} = 1) the droplets started to self-organize within seconds. The organization manifested in the formation of hundreds of geometrically close-packed clusters containing dozens of droplets each, where EFB droplets were encircled by BrOct droplets (**Figure 1c-i, Video S1**). The clusters translated, rotated, and exchanged droplets over time. Upon reducing d_{BrOct}/d_{EFB} to 0.4 while maintaining a constant N_{BrOct}/N_{EFB} = 1, the droplets instead formed chains and open loops containing approximately 8 to 20 drops of alternating species (**Figure 1c-ii, Video S2**). Close-packed clusters were not observed at this lower diameter ratio. When we fixed d_{BrOct}/d_{EFB} = 0.4 but increased N_{BrOct}/N_{EFB} = 10, we observed yet another qualitatively distinct pattern: Each EFB droplet was surrounded by a geometrically close-packed monolayer of BrOct droplets, forming flower-like organizations (**Figure 1c-iii**).

In all cases, the patterns formed by the droplets reached a dynamic steady state that lasted for about 10 to 20 minutes, wherein the qualitative patterns remained the same, but each cluster or chain could exchange droplet constituents over time. We emphasize that the self-organization of these droplets is only possible when fueled by chemical gradients out-of-equilibrium, which is distinct from thermodynamically driven colloidal self-assembly. At equilibrium, the BrOct solubilized and disappeared, and activity was no longer observed. Overall, these preliminary tests showed that within this one simple chemical system, variations in the physical input parameters such as droplet diameter ratio and droplet number ratio could lead to distinctly different qualitative organizational patterns.

We were motivated to more systematically explore how different combinations of droplet diameter ratios and number ratios affect the steady state patterns. Empirically, we found that number densities of 50 to 100 droplets per mm^2, which corresponds to roughly 2,000 to 4,000 droplets in the camera's field of view when using a 2x objective, was optimal; larger densities resulted in droplet crowding, while lower densities led to minimal droplet interactions due to the large distances between neighbors. Going forward, we therefore kept the number density consistent in this range while varying d_{BrOct}/d_{EFB} between 0.5 and 2.0 and varying N_{BrOct}/N_{EFB} between 0.1 and 10. Experiments were conducted as described previously, wherein monodisperse BrOct and EFB droplets of desired radii and relative numbers were dispersed in 0.5 wt% TX-100, and their organization was monitored over time by optical microscopy.

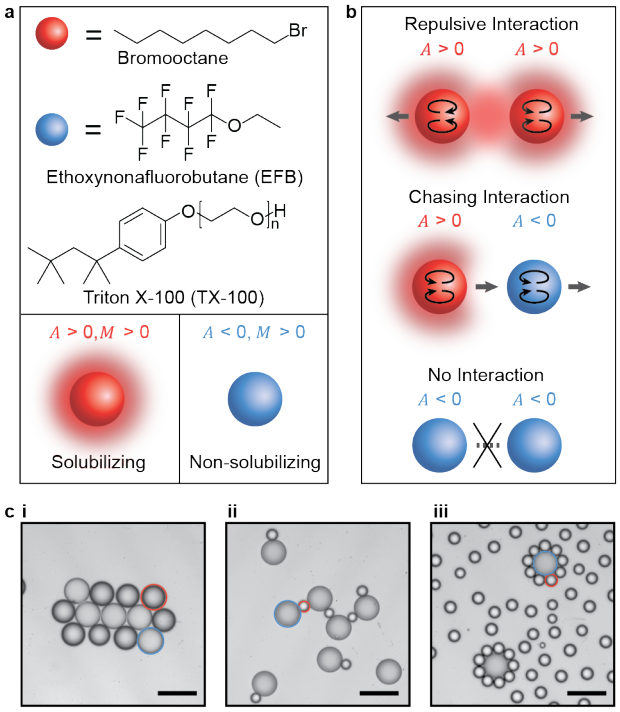

Figure 1. Chasing droplets self-organize into qualitatively different patterns as a function of droplet diameter ratio and number ratio. (a) Chemical structures of the two types of oil droplets, bromooctane (BrOct) and ethoxynonafluorobutane (EFB), and the surfactant, Triton X-100 (TX-100) where average n = 9 to 10. Activity (A) defines how droplets modify a solute gradient and mobility (M) describes how droplets respond to a solute gradient. The gradient shading around the droplet represents gradients of oil-filled micelles. In 0.5 wt% TX-100 surfactant solution, BrOct droplets solubilize (A > 0) while EFB droplets uptake the solubilizate from BrOct (A < 0), and both droplets move towards a lower concentration of solubilized oil (M > 0). **(b)** Schematics of the pairwise interactions formed by droplets with M > 0 and different values of A. BrOct droplets repel each other, BrOct chases EFB (i.e., a non-reciprocal interaction), and EFB droplets have no interaction. Higher concentrations of oil filled micelles near the interface correlate to higher interfacial tensions. The corresponding Marangoni flow direction within each droplet is drawn. **(c)** Droplets self-organize into diverse patterns at different

diameter ratios and number ratios of BrOct and EFB in 0.5 wt% TX-100. Red and blue outlines identify the BrOct and EFB, respectively. Scale, 100 μm. **(c-i)** d_{BrOct}/d_{EFB} = 1 and N_{BrOct}/N_{EFB} = 1. Clusters of EFB droplets are encircled by BrOct droplets (**Video S1**). **(c-ii)** d_{BrOct}/d_{EFB} = 0.4 and N_{BrOct}/N_{EFB} = 1. BrOct and EFB droplets alternate in chains and loops (**Video S2**). **(c-iii)** d_{BrOct}/d_{EFB} = 0.4 and N_{BrOct}/N_{EFB} = 10. Each EFB droplet is fully surrounded by BrOct droplets, forming a flower-like pattern.

When d_{BrOct}/d_{EFB} was fixed at 0.5 and N_{BrOct}/N_{EFB} increased from 0.1 to 1 to 10, droplets transitioned from chains to core-shell close-packed clusters (**Figure 2a-i**) largely analogous to what was shown in **Figure 1c**. For example, at N_{BrOct}/N_{EFB} = 0.1 to 1, smaller BrOct droplets coordinated two larger EFB to form chains and loops, while at higher N_{BrOct}/N_{EFB} = 10, each EFB was coordinated by 8 BrOct droplets, forming a flower. Transition between these patterns was gradual, with a mixture of patterns forming with number ratios between these values along the continuum. Interestingly, at the lower values of N_{BrOct}/N_{EFB} (**Figure 2a-i**, N_{BrOct}/N_{EFB} = 0.1), where there was a large excess of EFB, the EFB drops appeared to be slightly attractive [47]. We believe this unexpected attraction between the EFB, which does not happen for EFB drops on their own, results from the fact that there is solubilized BrOct oil in the aqueous phase; since EFB is a sink for BrOct, there will be less BrOct solute between the EFB causing them to attract. This attractive behavior was recapitulated by placing EFB into 0.5 wt% TX-100 saturated with BrOct oil.

If N_{BrOct}/N_{EFB} was constant at 10 and d_{BrOct}/d_{EFB} varied between 0.5 and 2, we saw consistent manifestation of flower patterns with a core of EFB and a shell of BrOct, irrespective of the diameter ratio (**Figure 2a-ii**). However, the number of BrOct drops surrounding each EFB decreased as d_{BrOct}/d_{EFB} increased, governed by geometric constraints. When d_{BrOct}/d_{EFB} fell in a range where, geometrically, the BrOct drops were just a little too large to be fully close-packed, one of the BrOct droplets could be offset and not touch the EFB (**Figure S1**). The effective net attraction between the EFB and BrOct apparently overpowered the pairwise repulsion of the BrOct to enable the formation of these close-packed flowers.

A schematic diagram summarizing the different pattern morphologies that are obtainable after varying combinations of d_{BrOct}/d_{EFB} and N_{BrOct}/N_{EFB} is presented in **Figure 2b** (**Video S3**). Qualitatively consistent patterns were observed when ratios fell around values indicated in each grid while for transitionary compositions, mixtures of patterns were obtained (**Figure S2**). Some other interesting behaviours were observed in some extended regions, for example, under the condition of d_{BrOct}/d_{EFB} = 3.0 and N_{BrOct}/N_{EFB} = 0.05, BrOct droplets rapidly contacted and exchanged different EFB, leaving self-avoiding tracks behind in their wake (**Video S4**).

Non-reciprocal chemotactic framework for conceptually rationalizing pattern formation trends

An overarching takeaway from **Figure 2b** is that while we commonly found geometrically close-packed clusters and flowers with EFB cores, we never observed close-packed clusters and flowers with BrOct cores. Even when the EFB were smaller and far outnumbered the BrOct (e.g. d_{BrOct}/d_{EFB} = 2, N_{BrOct}/N_{EFB} = 0.1), a situation where it may be expected that the smaller EFB droplets readily surround the BrOct to maximize contact points, we did not observe close packing. A similar trend is also predicted by a computational model, which will be discussed later. We believe this non-commutative property of cluster organization is also what drives the formation of geometrically "loose" packed patterns like chains and loops. We attribute it to the fact that the effective force that brings the droplets together results from a nonreciprocal interaction, rather than a pairwise attraction. Conceptually, consider that when the BrOct and EFB droplets touch and exhibit an effective net attraction that holds them in contact, this represents a situation where the predator BrOct "catches" the EFB prey (i.e. a "successful chase"). Analogously, many predators can simultaneously chase, surround, and catch a single prey when prey are scarce ($N_{predator} \gg N_{prey}$), leading to EFB-core, close-packed clusters. However, a single predator cannot successfully chase many prey at once ($N_{predator} \ll N_{prey}$) leading to loose packing (**Figure 2c**). In instances where there are equal numbers of predators and prey ($N_{predator} \approx N_{prey}$), the pattern is more sensitive to diameter ratio; BrOct-bordered clusters are only achieved when $d_{BrOct} > d_{EFB}$.

Chemically, we rationalize this aforementioned trend as follows. BrOct predators act as the oil source, emitting at a certain solubilization rate, and the solubilized oil is transferred into the prey EFB sinks. This transfer sets up the chemical gradients necessary for the Marangoni flows that lead to chasing. For every additional EFB droplet that a BrOct drop catches, we imagine that the emitted BrOct oil available to transfer per EFB droplet is depleted, weakening the net chemotactic interaction. If too many EFB drops surround a BrOct, a failed chase results (**Figure 2c**). But, apparently, BrOct can at least catch two prey EFB simultaneously, which is the minimal requirement to stabilize a chain. In scenarios where there are more predators than prey ($N_{predator} > N_{prey}$), irrespective of the specific diameter ratio, BrOct predators can completely encircle each prey EFB, where the net transfer of oil from BrOct to the EFB core apparently is sufficient to overcome the net repulsive chemotactic interactions between BrOct. However, the repulsive interactions between the BrOct droplets do still prevent formation of a second layer of BrOct droplets around the cluster edge, and so the cluster size is self-limiting.

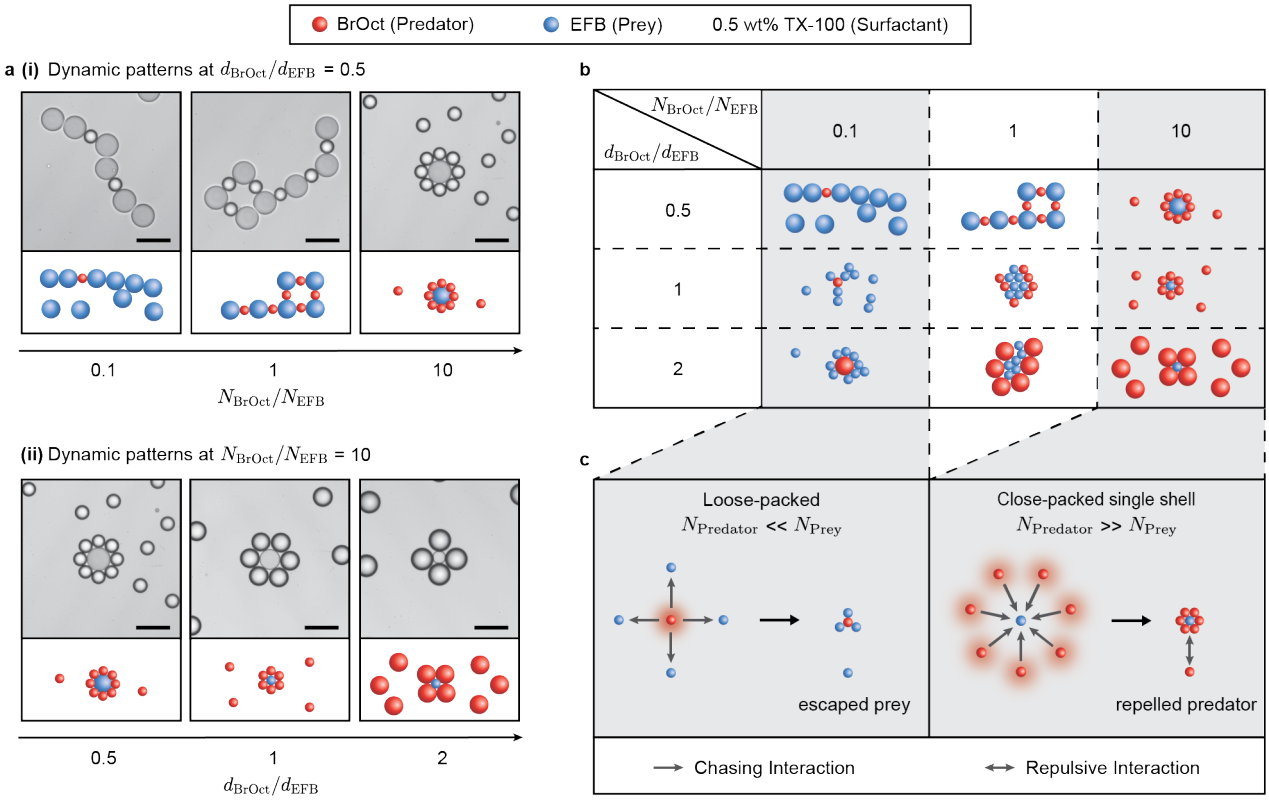

Figure 2. Diverse patterns of self-organizing droplets formed at different drop diameter ratios (d_{BrOct}/d_{EFB}) and number ratios (N_{BrOct}/N_{EFB}). Red and blue spheres represent BrOct and EFB droplets respectively. All experiments were conducted in 0.5 wt% TX-100. **(a-i)** Optical micrographs of self-organized patterns at d_{BrOct}/d_{EFB} = 0.5 for N_{BrOct}/N_{EFB} = 0.1, 1, and 10. **(a-ii)** Optical micrographs of self-organized patterns at N_{BrOct}/N_{EFB} = 10 for d_{BrOct}/d_{EFB} = 0.5, 1, and 2. Patterns shown in the micrographs are dynamic and can reorganize over time while keeping the same general morphology. Scale, 100 μm. **(b)** Schematic representations of how the experimentally determined patterns vary as a function of N_{BrOct}/N_{EFB} and d_{BrOct}/d_{EFB}. See **Video S3**. **(c)** Conceptual representation of how the droplet non-reciprocal chemotactic interactions lead to the formation of geometrically loose-packed or close-packed patterns. Red shading depicts gradients of the predator (source) oil. Single-headed arrows represent a chasing interaction and double-headed arrows represent a repulsive interaction. For $N_{Predator} \ll N_{Prey}$, each predator (source) is surrounded by a variable number of prey (sinks) but no close-packed structure forms as only a limited number of prey can be captured by one predator. When $N_{Predator} \gg N_{Prey}$, predators (source) completely encircle the prey (sink) and form patterns that are geometrically close-packed. Other predators are repelled by the formed single-layer shell and cluster size is self- limiting.

Quantitative analysis of the emergent patterns

Given the variety of emergent self-organized patterns that were qualitatively observed in **Figure 2**, we devised metrics to quantify these organizations and explore how the dynamics of the droplets vary between these situations. To quantitatively investigate the pattern formation, we calculated the average number of BrOct neighbors around an EFB droplet using the procedure described below. The lengths of the trajectories analyzed in the present work is 392 frames. At an image acquisition rate of 0.5 frames per second, the total length of each video is 784 seconds. The number of droplets present within the field of view of the microscope could vary from frame to frame even though the overall number density in the whole dish was conserved. For the neighbor calculation procedure, therefore, we only considered those EFB droplets which were present in all the 392 frames. The total number of BrOct that was in contact with each EFB droplet at each timepoint was recorded. The maximum number of BrOct neighbors that the i^{th} EFB drop experienced during its existence in the time series is denoted by $N_i^{\mathrm{max-BrOct}}$. To mitigate the effects of transient fluctuations on the process of neighbor counting, we required that the value $N_i^{\mathrm{max-BrOct}}$ persist for at least 20 frames in the time series. The analysis was repeated for all the EFB droplets, and the ensemble-averaged value for the maximum BrOct neighbors around an EFB droplet is then given by

$$\mu_{EFB}^{BrOct} = \frac{1}{N_{EFB}} \sum_{i=1}^{N_{EFB}} N_i^{\mathrm{max-BrOct}} \qquad (1)$$

An illustration of this calculation for an experimental dataset is shown in **Figure S3.** We plotted $\mu_{\mathrm{EFB}}^{\mathrm{BrOct}}$ as a function of N_{BrOct}/N_{EFB} and d_{BrOct}/d_{EFB} (**Figure 3a**). A general trend observed across the various d_{BrOct}/d_{EFB} is that the average number of BrOct neighbors surrounding an EFB droplet increases with N_{BrOct}/N_{EFB}. The number of neighbors must plateau with the geometrical limit set by the diameter ratio. We observe that this plateau is reached around a number ratio of 10 for each diameter ratio. The dynamics of pattern formation were quantified using a motility function by adapting a methodology that has recently been used to study the motion of chloroplasts [7]. We define the motility function $Q(t)$ at a given time instance t, as

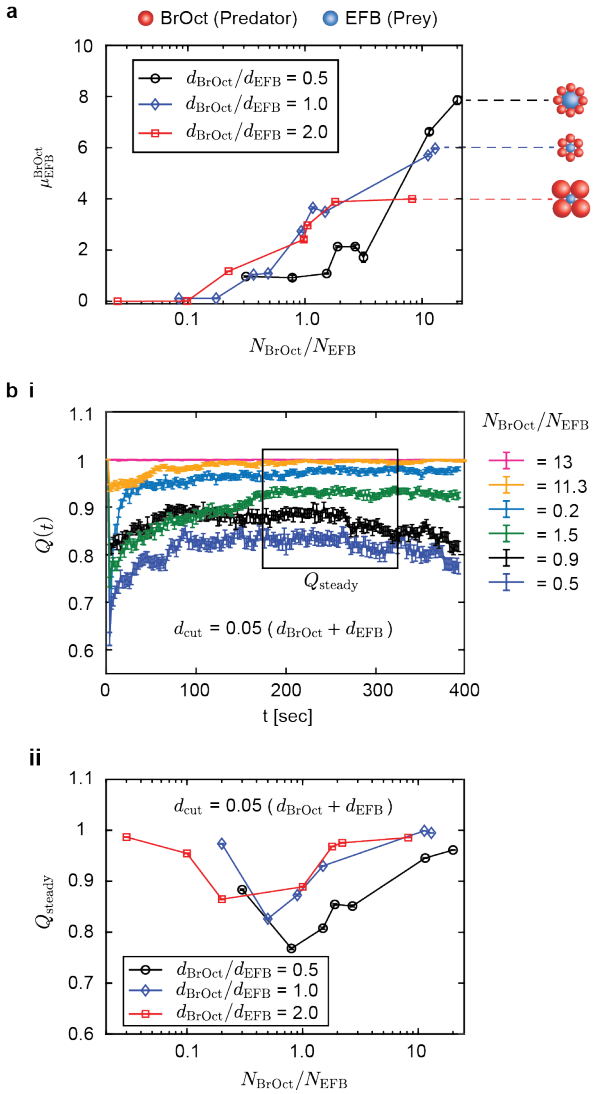

Figure 3. Structures and motilities of patterns formed in 0.5 wt% TX-100 solution were quantified at various N_{BrOct}/N_{EFB} and d_{BrOct}/d_{EFB}. (a) Maximum numbers of BrOct droplets surrounding a EFB droplet on average, $\mu_{\mathrm{EFB}}^{\mathrm{BrOct}}$, are plotted as a function of N_{BrOct}/N_{EFB} for various d_{BrOct}/d_{EFB}. The highest $\mu_{\mathrm{EFB}}^{\mathrm{BrOct}}$ corresponds to flower patterns (drawn in schematic). Error bars, which are smaller than symbol size, represent the standard error of the mean. The error bars are evaluated from experiments with a sample size ranging from 26 to 1380 EFB droplets. **(b)** Motility function analysis of experiments. The cut-off distance d_{cut} was set as $0.05(d_{BrOct} + d_{EFB})$ after testing for convergence. **(b-i)** Time-sequence trajectories of the motility function $Q(t)$ at $d_{BrOct}/d_{EFB} \approx 1$ and several different values of N_{BrOct}/N_{EFB}. Q_{steady} is calculated by averaging over the framed 150-second window. Error bars represent the standard error of the mean. The error bars are evaluated from experiments with a sample size ranging from 379 to 2582 total number of droplets. **(b-ii)** Steady-state values of the motility function, Q_{steady}, are plotted as a function of N_{BrOct}/N_{EFB} for various d_{BrOct}/d_{EFB}. Error bars, which are smaller than symbol size, represent the standard error of the mean.

$$Q(t) = \frac{1}{N}\sum_{i=1}^{N} H(d_{cut} - \sigma_i(t)) \qquad (2)$$

where $N \equiv N_{BrOct} + N_{EFB}$ is the total number of droplets, $H(x)$ is the Heaviside function with $H(x) = 1$ for $x > 0$ and 0 otherwise, and $\sigma_i(t)$ denotes the displacement of the i^{th} droplet measured with respect to the previous timestep. The motility function is therefore an estimate of the number of droplets that have moved a distance greater than the cut-off distance d_{cut} at a given time and is normalized to lie between zero and one. A high (low) value of $Q(t)$ indicates a relatively smaller (larger) displacement of the droplet relative to the cut-off distance, on average. A detailed discussion on the sensitivity of the motility function to the choice of d_{cut} is provided in the Supporting Information section "Quantitative Analyses" and illustrated in **Figure S4**. The motility function $Q(t)$ was plotted in a time series for the case of $d_{BrOct}/d_{EFB} \approx 1$ and various values of N_{BrOct}/N_{EFB} (**Figure 3b-i**). We calculated the steady state value of the motility function (Q_{steady}) by time-averaging over a 150-second window and found that Q_{steady} varied non-monotonically with N_{BrOct}/N_{EFB} (**Figure 3b-ii**). A minimum in Q_{steady} (maximum motility) was observed when there are equal numbers of both droplets, $N_{BrOct}/N_{EFB} \approx 1$, because it maximizes the number of motile pairs that can be formed. This trend was preserved for all the three d_{BrOct}/d_{EFB} examined. Furthermore, it appears that systems with larger EFB droplets are more motile.

A minimal computational model simulating the pattern formation

Having defined the metrics to quantify the structure and dynamics of pattern formation in source-sink droplet systems, we next sought to develop a minimal computational model and see whether the experimentally observed trends could be recapitulated. We used a "dry" model [42,44,46] of chemotactic disks that ignores hydrodynamic interactions. The disks are confined to motion in a two-dimensional plane, analogous to the experiments in which droplets are settled at the bottom of a dish. The micelles emitted from experimental droplets diffuse in three dimensions [46], and this diffusion is faster than the motion of the droplets. Therefore, a quasi-steady concentration field develops around an isolated droplet in three dimensions that obeys the following functional form

$$(c(r) - c_0) = \frac{A_s}{r}, \qquad (3)$$

where c_0 represents the reference concentration far from the droplet and A_s is the activity coefficient, and r is the distance to the droplet's center. The subscript "s" denotes the type of species (source or sink), and the activity coefficient is positive (negative) for the source (sink) species. The products of solubilization interact phoretically with the surface of the disks, such that the velocity of a droplet of species "s" in response to the chemical field is given by $\boldsymbol{v}_s = -M_s \nabla c$, where M is the mobility coefficient, and a positive (negative) value of the mobility indicates that the droplet moves to a region of lower (higher) concentration. Combining the expression for the phoretic velocity with the concentration profile given by **Equation 3**, and when micelle transport due to advection is slow compared to micelle diffusion [48], the velocity of a droplet of species *j* due to the presence of droplet of species *i* may be written as [42,44,46]

$$\boldsymbol{v}_{ij} = A_i M_j \left(\frac{\boldsymbol{r}_{ij}}{r_{ij}^3}\right);\ \boldsymbol{r}_{ij} = \boldsymbol{r}_j - \boldsymbol{r}_i. \tag{4}$$

We consider a total of $N \equiv N_{BrOct} + N_{EFB}$ disks in our simulations. The simulation parameters are specified in dimensionless units. The disks are confined in a periodic square box of side length L. Their positions evolve in time according to

$$\frac{d\boldsymbol{r}_m}{dt} = \sum_{n\neq m}^{N} \boldsymbol{v}_{nm} + \sum_{m=1}^{N} \boldsymbol{v}_m^{\mathrm{HM}}, \tag{5}$$

and **Eq. 5** is integrated using the explicit Euler algorithm with a discrete timestep width of $\Delta t = 0.1$. This choice of $\Delta t = 0.1$ ensures that no disk moves more than its own diameter during a timestep. The first term on the righthand side of **Eq. 3** is the chemotactic velocity of the m^{th} disk due to pairwise interactions with all the other disks in the box. The second term on the righthand side of **Eq. 5** models steric-repulsion using the Heyes-Melrose algorithm [49], and has the following functional form:

$$\boldsymbol{v}_m^{\mathrm{HM}} = \frac{0.5}{\Delta t}\sum_{k=1}^{n_o}(r_{mk} - d)\Theta(d - r_{mk})\hat{\boldsymbol{r}}_{mk}, \tag{6}$$

where n_o is the number of overlapping particles in the neighbourhood of the m^{th} particle, Θ denotes the Heaviside function, and $\hat{\boldsymbol{r}}_{mk} = \boldsymbol{r}_{mk}/r_{mk}$ is the unit vector along the line joining the particle centers. Two values of N are considered in the present work, N = 550 and N = 990. The sides of the simulation box are taken to be L = 20 and L = 35 respectively. These choices ensure that the area fractions of disks in the computer simulations are similar to that measured in experiments.

In simulations with periodic boundary conditions, particles that leave the box (of side L) through one boundary are presumed to re-enter through the opposite boundary. This effectively models an unbounded system in which the simulation box is repeated infinitely in both the spatial dimensions. We have adopted the minimum-image convention to model the interparticle interactions, in which each particle is presumed to "see" only its nearest periodic image, i.e., the largest interparticle interaction distance in either the x or y directions is not allowed to exceed $L/2$. An alternative simulation procedure that accounts for interactions between a particle and all its periodic images involves the use of Ewald summation. Although the chemotactic interactions are long-ranged, the present study focuses on the formation of short-ranged structures. We have therefore adopted the minimum-image convention to describe the interaction between active droplets, rather than implementing an Ewald summation [44,46]. The rationale for neglecting hydrodynamic interactions in the computational model, and a detailed discussion on factors that distinguishes the present work from previous studies on source-sink droplet systems, are presented in the "Numerical simulations" section of the Supporting Information.

The signs of both the activity and mobility coefficients were chosen to be consistent with experiments: BrOct droplets emit oil ($A_{BrOct} > 0$) while EFB droplets absorb oil ($A_{EFB} < 0$), and both the BrOct and EFB droplets are repelled by solubilized oil ($M_{BrOct} > 0$, $M_{EFB} > 0$) [40,50,51]. Although the signs of activity and mobility were obvious, it was less clear what specific values of A and M represented the specific chemical makeup of the system. We fixed $A_{BrOct} = \sqrt{0.1}$, $M_{BrOct} = \sqrt{0.1}$, screened a range of $|A_{BrOct}/A_{EFB}|$ and M_{BrOct}/M_{EFB} values in the range [0.2,10], and examined the emergent patterns which were then compared to experiments. Based on the trends, we observed that the ratio of the activities of the two species had a notable impact on $\mu_{\mathrm{EFB}}^{\mathrm{BrOct}}$, while the ratio of mobilities had negligible effect **(Figure S5)**. We ultimately chose values of $A_{BrOct} = \sqrt{0.1}$, $A_{EFB} = -\sqrt{0.1}$, $M_{BrOct} = \sqrt{0.1}$, and $M_{EFB} = 0.1\sqrt{0.1}$, following the rationale described in the "Parameter selection for the dry chemotactic model" section of the Supporting Information.

The spatial patterns formed at various relative number and diameter ratios of the BrOct and EFB disks are illustrated in a pattern diagram (**Figure 4a**), which recapitulates the broad trends observed in experiments (**Figure 2**), including the transition from chain-like to flower-like patterns with increasing N_{BrOct}/N_{EFB}. For all the values of d_{BrOct}/d_{EFB} considered in our simulations, we note that only for the case of N_{BrOct}/N_{EFB} = 10 were the patterns observed to be time-invariant. For the remaining cases, the positions of the disks evolved continuously in time, and snapshots from the halfway point of the simulation run were used for generating the phase map in **Figure 4a.** The time evolution of the disk positions for two values of N_{BrOct}/N_{EFB} is illustrated in **Figure S6**.

The variation of $\mu_{\mathrm{EFB}}^{\mathrm{BrOct}}$ as a function of N_{BrOct}/N_{EFB} was calculated from simulations (**Figure 4b**), which can be compared to the experiments in **Figure 3a**. Here, we do find a difference between experiments and simulations. For simulations, $\mu_{\mathrm{EFB}}^{\mathrm{BrOct}}$ is independent of d_{BrOct}/d_{EFB}, while experiments show a dependence on d_{BrOct}/d_{EFB}. We suspect this difference may be due to the experimental activity coefficient (which is related to solubilization rate) being diameter-dependent, which is not captured in the numerical model. As noted prior and shown in **Figure S5b,** simulations do show that the activity ratio crucially determines $\mu_{\mathrm{EFB}}^{\mathrm{BrOct}}$, yet our simulations used a fixed activity ratio. Potential future refinements to the model could be scaling the activity ratio $|A_{BrOct}/A_{EFB}|$ of the two species by a factor proportional to the ratio of their sizes, d_{BrOct}/d_{EFB}.

The dynamics of the simulated trajectories were analysed using the steady-state value of the motility function Q_{steady} **(Figure 4c)**, similar to what was done for the experimental analysis (**Figure 3b**). **Figure 4c** shows that upon plotting Q_{steady} against N_{BrOct}/N_{EFB} for three different d_{BrOct}/d_{EFB}, we observe a non-monotonicity, with the collective motility peaking when the relative population of predator and prey species are roughly equal. This is the same result as achieved in experiments, so it is notable that the selection of model parameters to closely match experimentally observed spatial patterns also leads to realistic predictions for the dynamics of the collective. Unlike the experiments, however, there is no clear trend in the variation of Q_{steady} with the diameter ratio. Additional details pertaining to the calculation of $\mu_{\mathrm{EFB}}^{\mathrm{BrOct}}$ from simulation trajectories, the evaluation of the steady state value of the motility function obtained from simulations, as well as the sensitivity of Q_{steady} to the cut-off distance used in simulations, have been illustrated in **Figures S7-S8**.

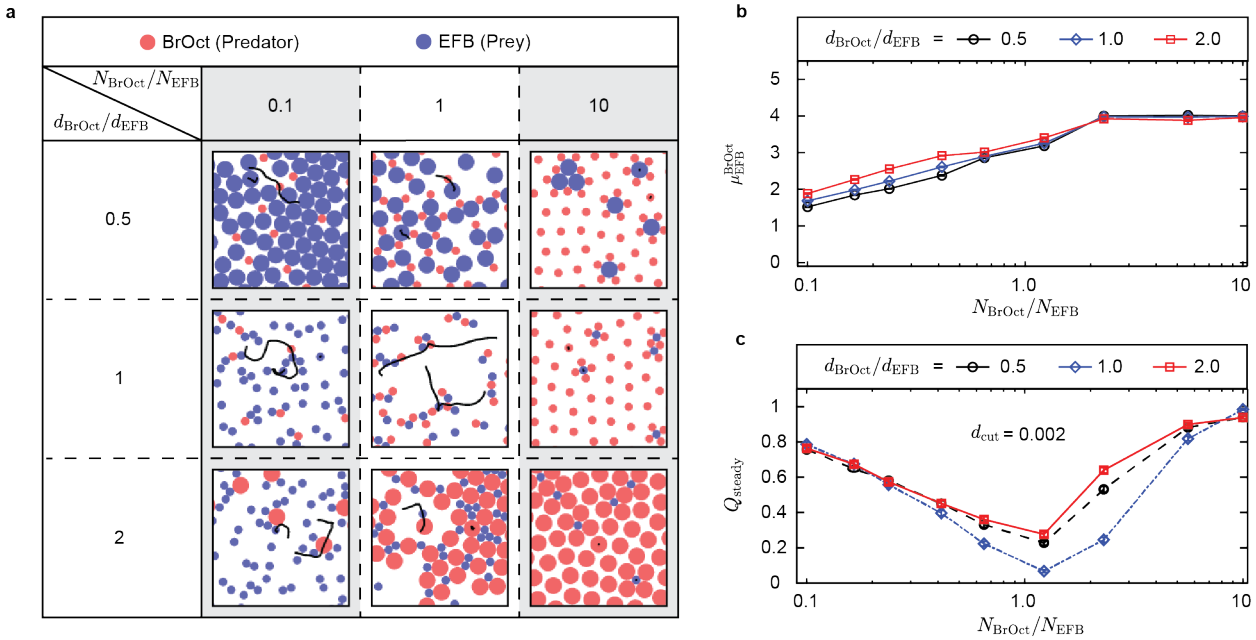

Figure 4. Emergent self-organization simulated using a computational model recapitulates experimental results. (a) The red and blue disks represent BrOct (predator) and EFB (prey) droplets, respectively, used in the simulation. Schematic representation of the simulated pattern diagram with different combinations of N_{BrOct}/N_{EFB} and d_{BrOct}/d_{EFB}. A total of N=550 disks (droplets) were simulated for each case, in a square periodic box of side L = 20. The simulations were performed for a total of 3000 steps, with a discrete timestep Δt = 0.1. The snapshots are taken at a dimensionless time of $t = 1500$, while the trajectory lines indicate the path traced by two exemplary disks, one of each type, in the interval from $t = 1400$ to $t = 1600$. **(b)** For simulated data, the maximum number of BrOct disks surrounding a central EFB disk on average, $\mu_{\mathrm{EFB}}^{\mathrm{BrOct}}$, plotted as a function of N_{BrOct}/N_{EFB} for various d_{BrOct}/d_{EFB}. Error bars, which are smaller than symbol size, represent standard error of the mean. The error bars are evaluated from simulations with a sample size ranging from 90 to 900 EFB disks. **(c)** Steady-state values of the motility function, Q_{steady}, evaluated from simulation trajectories, plotted as a function of N_{BrOct}/N_{EFB} for various d_{BrOct}/d_{EFB}. The cut-off distance d_{cut} is set as 0.002 after testing for convergence. Error bars, which are smaller than symbol size, represent the standard error of the mean. The error bars are evaluated from simulations with a sample size of 990 total number of disks.

Time evolution of self-organized patterns

The dynamic steady state patterns studied in this work were non-equilibrium and transient. Over time, the BrOct source droplets solubilized and the fuel dissipated. However, we noticed that in many cases, the pattern disintegration occurred long before the BrOct source droplets disappeared. For instance, for d_{BrOct}/d_{EFB} = 0.6 and N_{BrOct}/N_{EFB} = 10 in 0.5 wt% TX-100, close-packed and stable flowers formed within seconds, but after about 18 minutes, BrOct drops started detaching from the cluster. Shortly thereafter, the cluster fully disintegrated (**Figure 5a**). Most flower clusters in the field of view fell apart at approximately the same time (**Video S5**). We suspected that BrOct oil accumulation within the central EFB drop was the main factor determining this pattern disintegration, because the EFB drop does not have infinite capacity as a sink. Initially, the core EFB drop uptakes BrOct solubilizate, resulting in the accumulation of BrOct inside EFB. However, just as BrOct can transfer into EFB, it can also transfer out; as higher concentrations of BrOct are reached inside the EFB, the net oil transfer from BrOct to EFB becomes weaker. Eventually, there is not sufficient net transfer of BrOct into the EFB, and the cluster falls apart. This chemical transfer of BrOct into the EFB can be visualized over time using a change in drop refractive index [40] and correlated to the pattern disintegration. BrOct has a higher refractive index (n = 1.45) and EFB has a lower refractive index (n = 1.28); BrOct accumulation in the EFB thus raises the index of the EFB closer to that of water (n = 1.33). At d_{BrOct}/d_{EFB} = 2.0 and N_{BrOct}/N_{EFB} = 10, it is particularly noticeable how the refractive index of the central EFB drop increased with time (due to BrOct uptake) preceding the disintegration of the cluster, and the EFB became almost optically transparent (**Figure 5b**). After disintegration, the isolated EFB droplet's refractive index decreased over time, as BrOct solute was emitted from EFB to the surroundings (**Figure 5b**, t = 33 min).

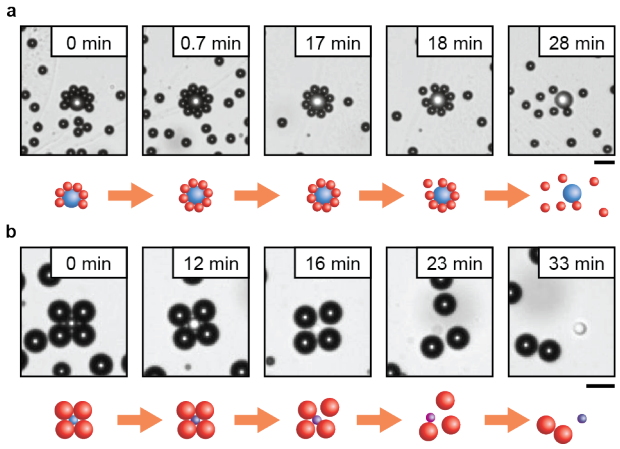

Figure 5. Time evolution of self-organized pattern disintegration. (a) Time-sequence frames and diagrams of one exemplary flower pattern at d_{BrOct}/d_{EFB} = 0.6 and N_{BrOct}/N_{EFB} = 10 in 0.5 wt% TX-100. Red spheres represent BrOct, and blue spheres represent EFB. The flower formed at t = 0.7 min and started breaking apart at t = 18 min. **Video S5** shows this behavior for many flower clusters across a larger field of view. **(b)** Similar to **(a)** but for a flower with one

EFB surrounded by four BrOct drops in 0.5 wt% TX-100 for d_{BrOct}/d_{EFB} = 2.0 and N_{BrOct}/N_{EFB} = 10. The refractive index of the center EFB (n = 1.28) increased over time by uptaking BrOct oil, which has a higher refractive index (n = 1.45). The refractive index of EFB decreased after dissociating from the cluster at longer times. In the schematics, the color of the EFB sphere is changed from blue to purple and back to blue to represent the change in oil composition upon BrOct transfer. Scale, 100 µm.

Self-organized patterns in mixed surfactant systems

Because TX-100 selectively solubilizes BrOct over EFB, in all prior experiments, BrOct was always the source (predator) and EFB the sink (prey). However, if a different surfactant is used, then which droplet is the source and sink as well as the strength of the interaction can be tuned [40]. For example, we previously showed that replacing TX-100 with a fluorosurfactant that preferentially solubilized the EFB led to a reversal in the drop chasing direction: EFB became the predator, and BrOct the prey [40]. We wondered how the self-organization would evolve in such a case where a different surfactant, or mixtures of surfactants, are used. To turn EFB into a source, we used 3 wt% aqueous Capstone FS-30 (Capstone), which is a non-ionic fluorinated surfactant that solubilizes EFB at a rate of 0.46 ± 0.03 µm/min (defined as change in diameter over time) (**Figure 6a**). We mixed different volume ratios of 0.5 wt% TX-100 and 3 wt% Capstone, with $f_{Capstone}$ representing the volume fraction of Capstone solution, and examined the droplet organizations at d_{BrOct}/d_{EFB} = 2 and N_{BrOct}/N_{EFB} = 0.1 (**Figure 6b**). Loose-packed clusters formed in TX-100 at $f_{capstone}$ = 0 as previously described. When mixing BrOct and EFB in 3 wt% Capstone solution ($f_{capstone}$ = 1), a close-packed flower pattern emerged that had a core of BrOct surrounded by EFB, which is inverted in comparison to the flower pattern observed under the inversed diameter ratio and number ratio (i.e. d_{BrOct}/d_{EFB} = 0.5 and N_{BrOct}/N_{EFB} = 10) in a 0.5% TX-100 solution (**Figure 2a**). This is reasonable, because when transitioning from TX-100 to Capstone surfactant, the predator and prey are swapped: BrOct acts as the prey, while EFB functions as the predator. In mixed surfactants, BrOct and EFB are both solubilizing, therefore neither of them can be purely defined as predator or prey. Competitive chases emerge from both species. We expected that an intermediate composition of surfactants could be achieved where there is almost no net oil transfer between droplets leading to minimization in non-reciprocal interactions and possibly net repulsive interactions. We found that $f_{Capstone}$ = 0.25 is closest to this point, where most droplets stayed separated and evenly spaced from each other, indicating weak repulsion (**Video S6**). Increasing $f_{Capstone}$ above 0.25, the number of nearest neighbours around each BrOct gradually increased from 0 to 7 (**Figure 6b**). Time-dependent cluster disintegration within mixed surfactant systems was observed as well (**Figure S9**).

Self-organized patterns in systems with multiple chasing interactions

After understanding the self-organization and pattern formation in the binary oil system, we wondered if hierarchical structures could be formed by adding a third species, for example, a flower pattern with two concentric shells. One possible embodiment is illustrated in **Figure 7a**, where blue drops chase red drops, and red drops

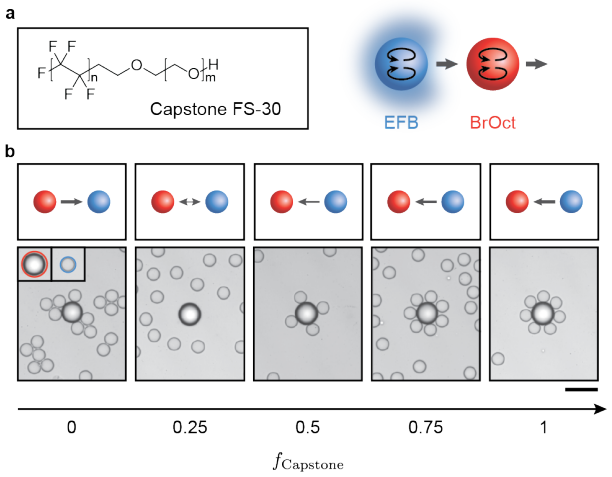

Figure 6. Swapping 0.5 wt% TX-100 with 3 wt% Capstone surfactant reverses the designation of predator and prey, while surfactant mixing enables tuning of the drop interactions. (a) Chemical structure of Capstone fluorosurfactant, which preferentially solubilizes the EFB such that EFB is now the predator, and BrOct the prey. **(b)** Representative optical micrographs showing how the self-organization changes upon mixing 0.5 wt% TX-100 and 3 wt% Capstone at different volume ratios. Red and blue circles represent BrOct and EFB droplets respectively. Droplets are mixed at d_{BrOct}/d_{EFB} = 2.0 and N_{BrOct}/N_{EFB} = 0.1. $f_{Capstone}$ represents the volume fraction of 3 wt% Capstone solution in the mixed surfactant solution, i.e. $f_{Capstone}$ = 1 corresponds to 3 wt% Capstone and $f_{Capstone}$ = 0 corresponds to 0.5 wt% Triton X-100. Diagrams show the chasing direction in different compositions of the surfactant. The thicker arrows represent stronger chasing interactions. Scale, 100 µm.

chase yellow drops. In this case, the number of yellow drops should be less than the other two species to form flower patterns. To test if this concept could work in practice, we designed a ternary system by adding a third oil droplet species along with BrOct and EFB droplets in a mix of TX-100 and Capstone (**Figure 7b**). As for our third "yellow" droplet, we needed an oil that would not solubilize in Capstone nor TX-100 and would be a sink for BrOct but not EFB. We chose to use halogenated hexadecane oil [40], because the long chain hexadecane does not solubilize in either surfactant, is fully miscible with the BrOct, and not fully miscible with EFB. In practice, we used a mixture of bromohexadecane and iodohexadecane with a volume ratio of 1:1 to tune the melting point well below room temperature and keep the density above 1 g/mL. The surfactant solution was composed of a mixture of 0.5 wt% TX-100 and 3 wt% Capstone with $f_{Capstone}$ = 0.5, where preferentially, EFB chased BrOct and BrOct chased the halogenated hexadecane oil. Upon mixing these three species of droplets, we observed flower patterns with a halogenated hexadecane core, surrounded by a first shell of BrOct, and a second shell of EFB (**Figure 7c-i**). For BrOct and EFB droplets not involved in the flower formation, they formed chains, which was favoured by the similar sizes and numbers of BrOct and EFB. Combinations of chains and flowers were also observed (**Figure 7c-ii**). The results indicate that this multi-droplet framework is extendable to more complex and hierarchical systems and can be used to rationally design self-organized patterns.

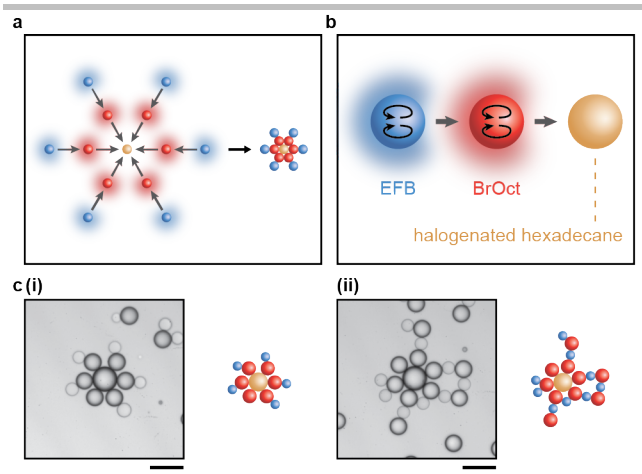

Figure 7. Flowers with two concentric shells formed in ternary oil systems. **(a)** Conceptual design of a hierarchical flower structure with two shells. Grey arrows represent the chasing interaction. **(b)** The chemical makeup of the ternary oil system that was tested. 0.5 wt% TX-100 and 3 wt% Capstone were added in equal volume. The third oil species, illustrated as a yellow sphere, was halogenated hexadecane (bromohexadecane and iodohexadecane mixed in equal volume). In this ternary system, EFB chases BrOct and BrOct chases the halogenated hexadecane oil droplet. Interaction between EFB and the hexadecane oil drop is very weak. **(c)** Representative optical micrographs of self-organized patterns. The number of BrOct and EFB drops were both about 10 times greater than that of the halogenated hexadecane oil drops. Scale, 100 μm. **(c-i)** Micrographs of a flower pattern with two shells, with BrOct in the first shell and EFB in the second shell. **(c-ii)** Loops formed by the BrOct and EFB connect the petals in the flower.

Conclusion

We have demonstrated a versatile chemical framework to direct self-organization in a multi-species mixture of chemotactically interacting oil droplets suspended in aqueous surfactant solutions. A variety of dynamic collective patterns, including flowers, chains, and clusters, result from tuning input factors such as droplet number ratios, diameter ratios, and surfactant compositions. The formed patterns can exchange droplets but maintain the same morphologies for minutes, which we designate as the dynamic steady state. During this period, the structures can be quantitatively characterized by the average number of neighbors and the motility of droplets through the metric Q_{steady}. Over longer timescales, the patterns disintegrate, and this process is linked to reduced oil transfer from the source (predator) to sink (prey) which weakens the strength of the chemotactic interaction between droplets. The motility analysis in the present work treats all droplets as equivalent in the system, without differentiating between isolated droplets and those that belong to a cluster. A more fine-grained analysis that accounts for this distinction could perhaps reveal additional insights about the origin of motility in such systems. Future work could focus on a more detailed cluster analysis, to find a correlation between the cluster size and motility of different patterns. A theoretical dry model framework was built using the minimal ingredients of chemotactic interaction and steric repulsion and reproduces the complex behaviors in terms of pattern formation and motility. Future refinements to the computational model may include time-dependent activities and variables dependent upon the droplet size. This conceptual framework is easily extended to more complex designs, where a ternary oil system with multiple chasing interactions and a more hierarchical flower pattern with two shells was demonstrated. More complex transport pathways could be harnessed in the future to create more sophisticated but rationalizable systems. Embedding the current framework with other well studied processes like droplets fueled by chemical reactions can provide opportunities for modelling activities in living cells or coacervates [52,53].

Supporting Information

Supporting information includes experimental details, detailed descriptions of the analytical methods, descriptions of the computational model, supporting figures, supporting videos with captions, link to the code used, compressed raw data files for analysis and additional references.

Acknowledgements

We gratefully acknowledge the support of the Charles E. Kaufman Foundation of the Pittsburgh Foundation (Grant 1031373-438639). L.Z. and Y.L. acknowledge support from the ARO (W911NF-18-1-0414) and the Alfred P. Sloan Foundation (500000010642). A. K. and R. K. acknowledge support from the Donors of the American Chemical Society Petroleum Research Fund (ACS-PRF 61858-ND9).

Keywords: Self-organization • Active Matter • Colloids • Non-reciprocity • Pattern formation

References

[1] D. P. Zitterbart, B. Wienecke, J. P. Butler, and B. Fabry, *Coordinated Movements Prevent Jamming in an Emperor Penguin Huddle*, PLoS ONE **6**, e20260 (2011).

[2] H. F. McCreery, G. Gemayel, A. I. Pais, S. Garnier, and R. Nagpal, *Hysteresis Stabilizes Dynamic Control of Self-Assembled Army Ant Constructions*, Nature Communications **13**, 1160 (2022).

[3] M. K. Faluweki, J. Cammann, M. G. Mazza, and L. Goehring, *Active Spaghetti: Collective Organization in Cyanobacteria*, Physical Review Letters **131**, 158303 (2023).

[4] Richard W. Castenholtz, *The Behavior of Oscillatoria Terebriforms in Hot Springs*, Journal of Phycology **4**, 132 (1968).

[5] U. Pfreundt, J. Słomka, G. Schneider, A. Sengupta, F. Carrara, V. Fernandez, M. Ackermann, and R. Stocker, *Controlled Motility in the Cyanobacterium Trichodesmium Regulates Aggregate Architecture*, Science **380**, 830 (2023).

[6] O. Hallatschek, S. S. Datta, K. Drescher, J. Dunkel, J. Elgeti, B. Waclaw, and N. S. Wingreen, *Proliferating Active Matter*, Nature Reviews Physics **5**, 407 (2023).

[7] N. Schramma, C. P. Israëls, and M. Jalaal, *Chloroplasts in Plant Cells Show Active Glassy Behavior under Low-Light Conditions*, Proceedings of the National Academy of Sciences of the United States of America **120**, e2216497120 (2023).

[8] G. Courcoubetis, M. S. Gangan, S. Lim, X. Guo, S. Haas, and J. Q. Boedicker, *Formation, Collective Motion, and Merging of Macroscopic Bacterial Aggregates*, PLoS Computational Biology **18**, 1 (2022).

[9] S. Osat and R. Golestanian, *Non-Reciprocal Multifarious Self-Organization*, Nature Nanotechnology **18**, 79 (2023).

[10] H. Zhao, A. Kosmrlj, and S. S. Datta, *Chemotactic Motility-Induced Phase Separation*, Physical Review Letters **131**, 118301 (2023).

[11] N. Ziethen, J. Kirschbaum, and D. Zwicker, *Nucleation of Chemically Active Droplets*, Physical Review Letters **130**, 248201 (2023).

[12] C. Luo and D. Zwicker, *Influence of Physical Interactions on Spatiotemporal Patterns*, Physical Review E **108**, 034206 (2023).

[13] S. Till, F. Ebmeier, A. A. Fragkopoulos, M. G. Mazza, and O. Bäumchen, *Motility and Self-Organization of Gliding Chlamydomonas Populations*, Physical Review Research **4**, L042046 (2022).

[14] M. Fruchart, R. Hanai, P. B. Littlewood, and V. Vitelli, *Non-Reciprocal Phase Transitions*, Nature **592**, 363 (2021).

[15] A. Dinelli, J. O'Byrne, A. Curatolo, Y. Zhao, P. Sollich, and J. Tailleur, *Non-Reciprocity across Scales in Active Mixtures*, Nature Communications **14**, 1 (2023).

[16] X. D. Pan and G. H. McKinley, *Characteristics of Electrorheological Responses in an Emulsion System*, Journal of Colloid and Interface Science **195**, 101 (1997).

[17] X. Shi, F. Cheng, and H. Chaté, *Extreme Spontaneous Deformations of Active Crystals*, Physical Review Letters **131**, 108301 (2023).

[18] A. Al Harraq, B. D. Choudhury, and B. Bharti, *Field-Induced Assembly and Propulsion of Colloids*, Langmuir **38**, 3001 (2022).

[19] M. Sun, W. Chen, X. Fan, C. Tian, L. Sun, and H. Xie, *Cooperative Recyclable Magnetic Microsubmarines for Oil and Microplastics Removal from Water*, Applied Materials Today **20**, 100682 (2020).

[20] R. S. Bang, L. Verster, H. Hong, L. Pal, and O. D. Velev, *Colloidal Engineering of Microplastic Capture with Biodegradable Soft Dendritic "Microcleaners,"* Langmuir **40**, 5923 (2024).

[21] A. Ghosh, W. Xu, N. Gupta, and D. H. Gracias, *Active Matter Therapeutics*, Nano Today **31**, 100836 (2020).

[22] X. Wang, Y. Yang, S. Roh, S. Hormozi, N. C. Gianneschi, and N. L. Abbott, *Self-Timed and Spatially-Targeted Delivery of Chemical Cargo by Motile Liquid Crystal*, Advanced Materials 2311311 (2024).

[23] W. Cui, J. Li, and G. Decher, *Self-Assembled Smart Nanocarriers for Targeted Drug Delivery*, Advanced Materials **28**, 1302 (2016).

[24] M. Li, M. Brinkmann, I. Pagonabarraga, R. Seemann, and J.-B. Fleury, *Spatiotemporal Control of Cargo Delivery Performed by Programmable Self-Propelled Janus Droplets*, Commun Phys **1**, 23 (2018).

[25] R. Zheng, Y. Wei, Z. Zhang, Z. Wang, L. Ma, Y. Wang, L. Huang, and Y. Lu, *Stimuli-responsive Active Materials for Dynamic Control of Light Field*, Responsive Materials **1**, e20230017 (2023).

[26] M. Rey, G. Volpe, and G. Volpe, *Light, Matter, Action: Shining Light on Active Matter*, ACS Photonics **10**, 1188 (2023).

[27] K. S. Khalil, A. Sagastegui, Y. Li, M. A. Tahir, J. E. S. Socolar, B. J. Wiley, and B. B. Yellen, *Binary Colloidal Structures Assembled through Ising Interactions*, Nature Communications **3**, 794 (2012).

[28] K. H. Li and B. B. Yellen, *Magnetically Tunable Self-Assembly of Colloidal Rings*, Applied Physics Letters **97**, 083105 (2010).

[29] F. Katzmeier, B. Altaner, J. List, U. Gerland, and F. C. Simmel, *Emergence of Colloidal Patterns in AC Electrical Fields*, Physical Review Letters **128**, 058002 (2022).

[30] J. I. Kach, L. M. Walker, and A. S. Khair, *Prediction and Measurement of Leaky Dielectric Drop Interactions*, Physical Review Fluids **7**, 013701 (2022).

[31] J. Kach, L. Walker, and A. Khair, *Nonequilibrium Structure Formation in Electrohydrodynamic Emulsions*, Soft Matter **19**, 9179 (2023).

[32] C. W. Shields and O. D. Velev, *The Evolution of Active Particles: Toward Externally Powered Self-Propelling and Self-Reconfiguring Particle Systems*, Chem **3**, 539 (2017).

[33] S. Michelin, *Self-Propulsion of Chemically Active Droplets*, Annual Review of Fluid Mechanics **55**, 77 (2023).

[34] A. Zöttl and H. Stark, *Modeling Active Colloids: From Active Brownian Particles to Hydrodynamic and Chemical Fields*, Annual Review of Condensed Matter Physics **14**, 109 (2023).

[35] S. Birrer, S. I. Cheon, and L. D. Zarzar, *We the Droplets: A Constitutional Approach to Active and Self-Propelled Emulsions*, Current Opinion in Colloid and Interface Science **61**, 101623 (2022).

[36] C. C. Maass, C. Krüger, S. Herminghaus, and C. Bahr, *Swimming Droplets*, Annual Review of Condensed Matter Physics **7**, 171 (2016).

[37] P. Dwivedi, D. Pillai, and R. Mangal, *Self-Propelled Swimming Droplets*, Current Opinion in Colloid & Interface Science **61**, 101614 (2022).

[38] C. Krüger, C. Bahr, S. Herminghaus, and C. C. Maass, *Dimensionality Matters in the Collective Behaviour of Active*, The Europen Physical Journal E **39**, 64 (2016).

[39] B. Vajdi Hokmabad, A. Nishide, P. Ramesh, C. Krueger, and C. Maass, *Spontaneously Rotating Clusters of Active Droplet*, Soft Matter **18**, 2731 (2022).

[40] C. H. Meredith, P. G. Moerman, J. Groenewold, Y. J. Chiu, W. K. Kegel, A. van Blaaderen, and L. D. Zarzar, *Predator–Prey Interactions between Droplets Driven by Non-Reciprocal Oil Exchange*, Nature Chemistry **12**, 1136 (2020).

[41] J. Grauer, H. Löwen, A. Be'er, and B. Liebchen, *Swarm Hunting and Cluster Ejections in Chemically Communicating Active Mixtures*, Scientific Reports **10**, 5594 (2020).

[42] V. Ouazan-reboul, J. Agudo-canalejo, and R. Golestanian, *Self-Organization of Primitive Metabolic Cycles Due to Non-Reciprocal Interactions*, Nature Communications **14**, 4496 (2023).

[43] A. Dinelli, J. O'Byrne, A. Curatolo, Y. Zhao, P. Sollich, and J. Tailleur, *Non-Reciprocity across Scales in Active Mixtures*, Nature Communications **14**, 7035 (2023).

[44] J. Agudo-Canalejo and R. Golestanian, *Active Phase Separation in Mixtures of Chemically Interacting Particles*, Physical Review Letters **123**, 018101 (2019).

[45] S. Saha, J. Agudo-Canalejo, and R. Golestanian, *Scalar Active Mixtures: The Nonreciprocal Cahn-Hilliard Model*, Physical Review X **10**, 41009 (2020).

[46] R. Soto and R. Golestanian, *Self-Assembly of Catalytically Active Colloidal Molecules: Tailoring Activity through Surface Chemistry*, Physical Review Letters **112**, 068301 (2014).

[47] C. M. Wentworth, A. C. Castonguay, P. G. Moerman, C. H. Meredith, R. V. Balaj, S. I. Cheon, and L. Zarzar, *Chemically Tuning Attractive and Repulsive Interactions between Solubilizing Oil Droplets*, Angewandte Chemie International Edition **16802**, (2022).

[48] P. G. Moerman, H. W. Moyses, E. B. Van Der Wee, D. G. Grier, A. Van Blaaderen, W. K. Kegel, J. Groenewold, and J. Brujic, *Solute-Mediated Interactions between Active Droplets*, Phys. Rev. E **96**, 032607 (2017).

[49] D. M. Heyes and J. R. Melrose, *Brownian Dynamics Simulations of Model Hard-Sphere Suspensions*, Journal of Non-Newtonian Fluid Mechanics **46**, 1 (1993).

[50] J. Anderson, *Colloid Transport By Interfacial Forces*, Annual Review of Fluid Mechanics **21**, 61 (1989).

[51] S. Michelin, E. Lauga, and D. Bartolo, *Spontaneous Autophoretic Motion of Isotropic Particles*, Physics of Fluids **25**, 061701 (2013).

[52] C. Donau and J. Boekhoven, *The Chemistry of Chemically Fueled Droplets*, Trends in Chemistry **5**, 45 (2023).

[53] E. Jambon-Puillet, A. Testa, C. Lorenz, R. W. Style, A. A. Rebane, and E. R. Dufresne, *Phase-Separated Droplets Swim to Their Dissolution*, bioRxiv doi: https://doi.org/10.1101/2023.07.18.549556 (2023).